Speed-Sensorless Vector Control of a Bearingless Induction Motor With Artificial Neural Network Inverse Speed Observer

Xiaodong Sun, Long Chen, Zebin Yang, and Huangqiu Zhu

***Abstract*—To effectively reject the influence of speed detection on system stability and precision for a bearingless induction motor, this paper proposes a novel speed observation scheme using artificial neural network (ANN) inverse method. The inherent subsystem consisting of speed and torque winding currents is modeled, and then its inversion is implemented by the ANN. The speed is successfully observed via cascading the original subsystem with its inversion. The observed speed is fed back in the speed control loop, and thus, the speed-sensorless vector drive is realized. The effectiveness of this proposed strategy has been demonstrated by experimental results.**

***Index Terms*—Artificial neural network (ANN) inverse, bearingless induction motor (BIM), speed-sensorless, vector control.**

I. Introduction

In recent years, there is an increasing interest in bearingless motors around the world [1]–[3]. Due to the similarity of structure between electric motors [4], [5] and magnetic bearings [6], a bearingless motor combine the functions of a motor and a magnetic bearing together within the same stator frame. They can simultaneously produce the radial suspension force and torque on the rotor so that there is no mechanical contact between the stator and rotor. On the one hand, the magnetic suspension offers the advantages of no friction, no abrasion, no lubrication, high rotational speed, and high precision, in comparison to mechanical contact [7], [8]. On the other hand, a bearingless motor has incomparable advantages of small size, light weight, low cost as compared to a conventional tandem structure consisting of magnetic bearings and a motor. Therefore, bearingless motors are becoming more and more suitable for widespread applications, such as high-speed turbo machineries, machine tool spindles, vacuum pumps, blood pumps, computer disk drives, energy storage flywheels, etc [9]–[11]. Up to now, various types of bearingless motors have been proposed, such as bearingless reluctance motors, bearingless induction motors (BIMs), bearingless switched reluctance motors, bearingless permanent magnet synchronous motors, etc [12]–[16]. In these types of bearingless motors, the BIM has been paid much attention since its advent because its rotor construction is relatively simple and robust, and the torque ripples and cogging torque are less [12].

Since the BIM is a multivariable, nonlinear, and coupled system, the vector control is a reasonable choice to control its speed independently from the radial suspension forces. However, for all high-performance vector-controlled BIMs, it is necessary to gain the accurate rotational speed information. Normally, this information is achieved by using mechanical sensors such as incremental encoders, which are the most common positioning transducers used today in industrial applications. Nonetheless, using mechanical sensors will cause several disadvantages, such as increasing size, cost, maintenance, hardware complexity, electrical susceptibility, and reducing reliability and robustness of the drive system [17]–[20]. Especially, mechanical sensors are unsuitable for the inherent high-speed performance of BIMs due to the unavoidable mechanical contact. Therefore, the considerable speed-sensorless control strategies are badly needed for solving the problems, and the investigation of the speed-sensorless operation is essential for the further development of BIMs.

For the conventional induction motors, various techniques have been proposed to estimate speed for sensorless drives, such as the direct computing method [21], Luenberger observers method [22], [23], extended Kalman filter (EKF) method [24], [25], and model reference adaptive system (MRAS) method [26], [27]. The direct computing method is a simplest method based on the angular velocity of rotor flux vector and slip calculation using the induction motor model, but the estimated speed accuracy is not very satisfactory due to the great sensitivity to parameters variations and noise in the drive. The Luenberger observers method is a deterministic estimator which assumes a linearized time-invariant motor model. The EKF method can make the online estimation of states while identifying the motor parameters simultaneously in a relatively short time interval. The Luenberger observers and EKF methods are robust to motor parameters variations or identification errors, but they require a great number of real-time computations and are much more

Manuscript received November 17, 2011; revised February 28, 2012; accepted May 19, 2012. Date of publication June 12, 2012; date of current version July 8, 2013. Recommended by Technical Editor G. Yang. This work was supported in part by the National Natural Science Foundation of China under Project 61104016, in part by the Natural Science Foundation of the Jiangsu Higher Education Institutions of China under Project 11KJB510002, and in part by the Priority Academic Program Development of Jiangsu Higher Education Institutions under Project 201106.

X. Sun was with the School of Electrical and Information Engineering, Jiangsu University, Zhenjiang 212013, China. He is now with the Automotive Engineering Research Institute, Jiangsu University, Zhenjiang 212013, China (e-mail: xdsun@ujs.edu.cn).

L. Chen is with the Automotive Engineering Research Institute, Jiangsu University, Zhenjiang 212013, China (e-mail: chenlong@ujs.edu.cn).

Z. Yang and H. Zhu are with the School of Electrical and Information Engineering, Jiangsu University, Zhenjiang 212013, China (e-mail: zbyang@ujs.edu.cn; 13775545135@163.com).

Digital Object Identifier 10.1109/TMECH.2012.2202123

complicated in practical realization. In the MRAS method, an error vector is made up from the two models' outputs which are both dependent on different motor parameters. By adjusting the parameter that influences one of the models, the error is driven to zero. Compared with the Luenberger observers or EKF method, the MRAS method has the advantage in the simplicity of used models. But it is unstable in low speed or around zero speed running because the model-based estimation technique is dependent on rotor-induced voltages which is very small and even vanish at zero stator frequency.

In this paper, a novel method of speed-sensorless vector control for a BIM based on artificial neural network (ANN) inverse method is proposed. The basic principle of the method is to obtain the inverse model of the speed subsystem which consists of a static ANN and some differentiators, and then to establish the speed observer by cascading the original subsystem with the ANN inverse model. Based on this speed estimation method, the speed-sensorless vector control system of the BIM is set up. Finally, the proposed control strategy is confirmed on a dSPACE DS1104 DSP-based data acquisition and control (DAC) system.

This paper is organized as follows. In Section II, we describe the principle of radial suspension force generation in BIMs. Then, we analyze the inherent subsystem, gain its inverse model, and obtain the speed observer using the inverse system method in Section III. In Section IV, an ANN inverse speed observer is constructed. In Section V, the speed-sensorless vector control system of the BIM is set up. In Section VI, experiments are carried out, and the performance of the BIM drive system is analyzed and discussed. Finally, some conclusions are given in Section VII.

II. Principle of Radial Suspension Force Generation

Suppose the pole-pair number of torque windings is p_1, and that of suspension force windings is p_2. When the rotating magnetic field produced by the two sets of windings satisfy the following three conditions: 1) $p_2 = p_1 \pm 1$, 2) the two magnetic fields have the same rotation direction, and 3) the currents in two sets of windings have the same frequency, then the interactive magnetic fields will produce radial suspension forces in the constant direction.

According to the electromagnetic field theory, there are two kinds of magnetic force, namely, Lorentz force and Maxwell force in the BIM. Besides the electromagnetic torque produced by Lorentz force just as it works in an induction motor, it also can generate radial suspension force. Compared with Lorentz force, Maxwell force, also named magnetic resistance force, is the main source of the radial suspension force in the BIM. Fig. 1 shows the principle of radial suspension force generation. The four-pole flux ψ_4 and two-pole flux ψ_2 are generated by the torque winding currents i_1 and suspension force winding currents i_2 in the N_4 and N_2 turns of stator windings, respectively. Under no-load balanced conditions, if a positive radial suspension force along the x-axis is needed, the torque winding current i_1 and suspension force winding currents i_2 are electrified as shown in Fig. 1. The flux density in the airgap 1 is increased, because both fluxes ψ_4 and ψ_2 are in the same direction. On the other hand, the flux density in the airgap 2 is decreased because fluxes ψ_4 and ψ_2 are in the opposite direction. Therefore, a positive suspension force F_x is produced in the x-axis direction only. If the direction of suspension force winding currents is reversed, the radial suspension force in negative x-axis direction will be generated. Suspension force F_y in the y-axis direction can be produced using electrically perpendicular two-pole suspension force winding currents distribution. So, the rotor can be suspended steadily in the central equilibrium position by adjusting the magnitude and direction of the suspension force winding currents.

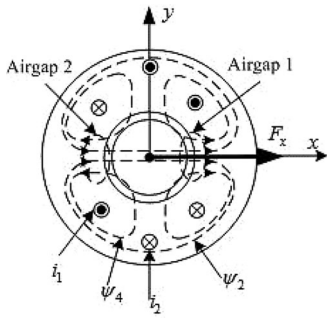

Fig. 1. Principle of radial suspension force generation.

III. Design of the Speed Observer

A. Left Inverse System

From the viewpoint of functional analysis, the dynamic model of a general system can be described as an operator mapping the inputs into the outputs. We consider a continuous system $\sum$ (linear or nonlinear) with a p-dimensional input vector $\boldsymbol{u}(t) = [u_1, u_2, \ldots, u_p]$, a q-dimensional output vector $\boldsymbol{y}(t) = [y_1, y_2, \ldots, y_q]$, and an initial state vector $\boldsymbol{x}(t_0) = \boldsymbol{x}_0$. Let $\theta : \boldsymbol{u} \rightarrow \boldsymbol{y}$ be the operator describing the aforementioned mapping relation, i.e., [28]

$$\boldsymbol{y}(\bullet) = \theta[\boldsymbol{x}_0, \boldsymbol{u}(\bullet)] \quad \text{or} \quad \boldsymbol{y} = \theta \boldsymbol{u}. \tag{1}$$

A system which can realize an inverse mapping from the output $\boldsymbol{y}$ to the input $\boldsymbol{u}$ can be defined as an inverse system or an inversion equivalently. In general, according to the difference of the function or purpose, the inverse systems can be divided into two classes, e.g., right inverse systems and left inverse systems. A right inverse system often serves as an output controller to make the output $\boldsymbol{y}$ of the original system to follow a given output, while the left inverse system serves as an input observer. Since what we are considered in this paper is studying effective observer approaches, all inverse systems refer to the left inverse systems hereafter if no special statement is given.

Definition 1: Consider a system $\sum$ expressed by (1). Assume Π to be another system with $\boldsymbol{y}(t)$ as input and $\boldsymbol{u}(t)$ as output, and it can be described by an operator $\bar{\theta} : \boldsymbol{y} \rightarrow \boldsymbol{u}$. If the operator $\bar{\theta}$ satisfies

$$\bar{\theta}\theta \boldsymbol{u} = \bar{\theta}\boldsymbol{y} = \boldsymbol{u} \tag{2}$$

the system Π is called the inverse system or inversion of the original system $\sum$, and the original system $\sum$ is invertible [29].

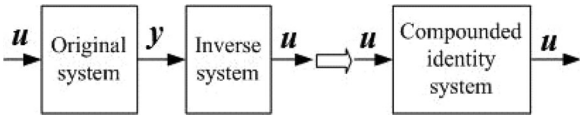

Fig. 2. Compounded identity system.

As shown in Fig. 2, by cascading the original system with such an inverse system, the compounded system would become an identity one, which means that the input of the original system can be gained from the output signal of such an inverse system. Since the inversion can completely reproduce the inputs of the original system, it can be treated as a soft sensor (or observer) to estimate some immeasurable variables.

B. Speed Observer Using Inverse System Method

The BIM is essentially an induction motor. For the motor system controlled inverter, under the assumptions of ignoring the nonlinear and time delay of the inverter, and magnetic circuit saturation and iron loss of the motor, a three-phase induction motor model according to the usual *d*-axis and *q*-axis components in a synchronous rotating frame with rotor flux orientation can be expressed by [30]

$$\begin{cases} \dot{i}_{s1d} = \dfrac{L_{m1}}{\sigma L_{s1}L_{r1}T_r}\psi_{r1d} - \dfrac{(R_{s1}L_{r1}^2 + R_{r1}L_{m1}^2)}{\sigma L_{s1}L_{r1}^2}i_{s1d} \\ \qquad\qquad +\omega_1 i_{s1q} + \dfrac{u_{s1d}}{\sigma L_{s1}} \\ \dot{i}_{s1q} = -\dfrac{L_{m1}}{\sigma L_{s1}L_{r1}}\omega_r\psi_{r1d} - \dfrac{(R_{s1}L_{r1}^2 + R_{r1}L_{m1}^2)}{\sigma L_{s1}L_{r1}^2}i_{s1q} \\ \qquad\qquad -\omega_1 i_{s1d} + \dfrac{u_{s1q}}{\sigma L_{s1}} \\ \dot{\psi}_{r1d} = -\dfrac{1}{T_r}\psi_{r1d} + \dfrac{L_m}{T_r}i_{s1d} \\ \dot{\omega}_r = \dfrac{p_1^2 L_{m1}}{JL_{r1}}\psi_{r1d}i_{s1q} - \dfrac{p_1}{J}T_L \end{cases} \tag{3}$$

where ψ_{r1d}, ψ_{r1q}, i_{s1d}, i_{s1q}, u_{s1d}, u_{s1q} are, respectively, the *dq*-axis components of the rotor flux linkage, stator current, and stator voltage of torque windings, ω_1 and ω_r are the synchronous and rotor electrical angular speed, respectively, L_{s1}, L_{r1}, and L_{m1} are the stator, rotor, and mutual inductances of torque windings, respectively, R_{s1} and R_{r1} are the stator and rotor resistances of torque windings, respectively, p_1 is the number of pole pairs of torque windings, J is the moment of inertia, $T_r = L_{r1}/R_{r1}$, and $\sigma = 1 - L_{m1}^2/(L_{s1}L_{r1})$.

State variables are chosen as

$$\boldsymbol{x} = [x_1, x_2, x_3, x_4]^{\mathrm{T}} = [i_{s1d}, i_{s1q}, \psi_{r1d}, \omega_r]^{\mathrm{T}}. \tag{4}$$

Input variables are chosen as

$$\boldsymbol{u} = [u_1, u_2]^{\mathrm{T}} = [u_{s1d}, u_{s1q}]^{\mathrm{T}}. \tag{5}$$

Output variables are chosen as

$$\boldsymbol{y} = [y_1, y_2]^{\mathrm{T}} = [x_3, x_4]^{\mathrm{T}} = [\psi_{r1d}, \omega_r]^{\mathrm{T}} \tag{6}$$

where the state variables x_1 and x_2 can be measured directly, and x_4 is the to-be-observed variable. In order to observe the rotor speed x_4, we may assume that, for the motor system (3), in its interior, there exists an inherent subsystem whose input is just the to-be-observed variable x_4, while outputs are the measurable state variables x_1 and x_2. As aforementioned, if the inherent subsystem is invertible, a compounded identity system would be obtained by cascading the subsystem with its inversion (i.e., inherent subsystem inversion), as shown in Fig. 3. Therefore, the inversion output is completely capable of reproducing the input of the inherent subsystem, i.e., the to-be-observed variable.

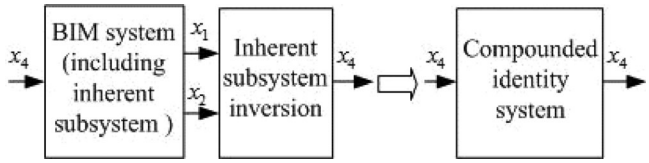

Fig. 3. Speed observation principle based on inverse system method.

According to the aforementioned constructing method of the subsystem model, the first and second equations of (3) are chosen as subsystem mathematical model, as rewritten as

$$\begin{cases} \dot{x}_1 = \dfrac{L_{m1}}{\sigma L_{s1}L_{r1}T_r}x_3 - \dfrac{(R_{s1}L_{r1}^2 + R_{r1}L_{m1}^2)}{\sigma L_{s1}L_{r1}^2}x_1 \\ \qquad\qquad +\omega_1 x_2 + \dfrac{u_1}{\sigma L_{s1}} \\ \dot{x}_2 = -\dfrac{L_{m1}}{\sigma L_{s1}L_{r1}}x_3 x_4 - \dfrac{(R_{s1}L_{r1}^2 + R_{r1}L_{m1}^2)}{\sigma L_{s1}L_{r1}^2}x_2 \\ \qquad\qquad -\omega_1 x_1 + \dfrac{u_2}{\sigma L_{s1}}. \end{cases} \tag{7}$$

That is, we can structure the inherent subsystem by selecting the state variables x_1 and x_2 and their derivatives $\dot{x}_1$ and $\dot{x}_2$. Thus, the reversibility of the inherent subsystem is needed to be proved.

Calculate the Jacobin matrix

$$\begin{aligned} \boldsymbol{A}(\boldsymbol{x}, \boldsymbol{u}) &= \begin{bmatrix} \dfrac{\partial \dot{x}_1}{\partial x_3} & \dfrac{\partial \dot{x}_1}{\partial x_4} \\ \dfrac{\partial \dot{x}_2}{\partial x_3} & \dfrac{\partial \dot{x}_2}{\partial x_4} \end{bmatrix} \\ &= \begin{bmatrix} \dfrac{L_{m1}}{\sigma L_{s1}L_{r1}T_r} & 0 \\ -\dfrac{L_{m1}x_4}{\sigma L_{s1}L_{r1}T_r} & -\dfrac{L_{m1}x_3}{\sigma L_{s1}L_{r1}T_r} \end{bmatrix}. \end{aligned} \tag{8}$$

So,

$$\mathrm{Det}(\boldsymbol{A}(\boldsymbol{x}, \boldsymbol{u})) = -\frac{L_{m1}^2}{\sigma^2 L_{s1}^2 L_{r1}^2 T_r}x_3. \tag{9}$$

Apparently, when $x_3 \neq 0$, and $\mathrm{Det}(\boldsymbol{A}(\boldsymbol{x}, \boldsymbol{u})) \neq 0$, $\boldsymbol{A}(\boldsymbol{x}, \boldsymbol{u})$ is nonsingular. According to the inverse function theory [31], under the condition $\mathrm{Det}(\boldsymbol{A}(\boldsymbol{x}, \boldsymbol{u})) \neq 0$, the system expressed in (7) is invertible, and based on implicit function theorem, its inversion can be expressed as

$$x_4 = \varphi(x_1, x_2, \dot{x}_1, \dot{x}_2, \omega_1, \boldsymbol{u}). \tag{10}$$

Fig. 4 shows the schematic diagram of rotor speed observation based on the inverse system method. From Fig. 4, it can be seen

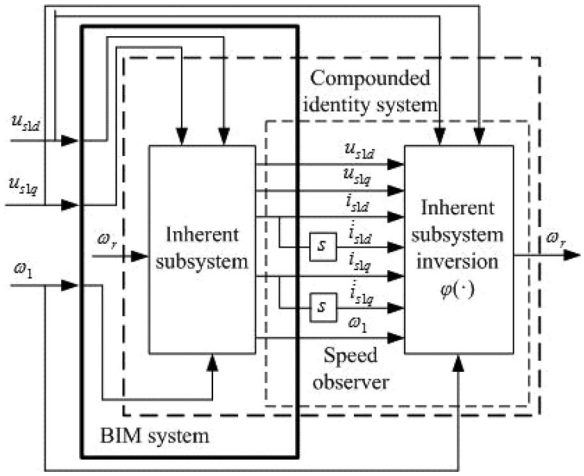

Fig. 4. Schematic diagram of speed observer using inverse system method.

that the speed observer consists of a nonlinear function $\varphi(\cdot)$ and two differentiators.

IV. Speed Observer Based on ANN Inverse

Obviously, the key to constructing the speed observer is by realizing the function $\varphi(\bullet)$. The real analytical inversion, i.e., the expression of the function $\varphi(\bullet)$ can precisely be obtained if the BIM system's mathematical model described in (3) is completely known. However, in practical engineering application, the BIM system usually has different working modes with respect to different running states, resulting the nonlinear characteristics of motor system very complex. The motor parameters such as the flux linkage, resistances, and inductances change very prominently with the time-varying conditions, so these parameters are not precisely known and are usually gained by parameter identification. In a word, it is difficult to get the accurate mathematical model of (3), and accordingly, the precise inversion model $\varphi(\bullet)$ cannot be easily obtained. Hence, direct realization of the imprecise inversion will inevitably lead to incorrect speed observation result.

Since the ANN has the ability of expressing arbitrary nonlinear mapping, learning, and self-adapting, we can make use of an ANN to approximate the nonlinear function $\varphi(\bullet)$ to break through the bottleneck in implementing the inverse system. Because $\varphi(\bullet)$ is a static nonlinear function, any kind of static ANN, such as back propagation, radial basis function, and its relevant learning algorithm, can be used to approximate the nonlinear function. Without loss of generality, we adopt a very common static ANN such as feedforward multilayer ANN in this paper. Taking the Kolmogorov theory [32] and the calculating ability of the computer into account, a feedforward multilayer ANN of $N^3_{6,13,1}$ is selected, where 3 represents layers of the ANN, 6 represents the number of the input layer neuron, 13 represents the number of the hidden layer neuron, and 1 represents the number of the output neuron. The activation functions for hidden neurons are tangent sigmoid functions, and the functions on the output layer nodes are linear. The Levenberg–Marquardt algorithm [33] is used in ANN training. After the feedforward multilayer ANN is trained with the training sample sets, it can be used together with the differentiators as the ANN inverse speed observer, where the differentiators represent the system dynamics to approximate $\varphi(\bullet)$.

The static ANN and the differentiators in the ANN inverse speed observer make up a specific type of dynamic ANN which is different from the ordinary dynamic ANN, for instance, the well-known Hopfield neural network consisting of dynamic neurons [33]. In this paper, the dynamic characteristic of the ANN inverse speed observer is accomplished by the differentiators. When approximating the nonlinear function $\varphi(\bullet)$, the static ANN and the differentiators play their individual roles in a relatively independent manner; therefore, the ANN inverse can achieve the speed observer with a correspondingly compact structure and legible mathematical meaning.

According to the procedures of ANN inverse control [34], the training samples of the static ANN are needed to be obtained first, and then, the ANN can be trained by the Levenberg–Marquardt algorithm. The training sample is made up of $\{u_{s1d}, u_{s1q}, i_{s1d}, \dot{i}_{s1d}, i_{s1q}, \dot{i}_{s1q}\}$ and $\{\omega_r\}$, which are the inputs and output of the static ANN, respectively.

V. Speed-Sensorless Vector Control

As for the control of radial suspension forces in the BIM, it can be realized by detecting the rotor's radial displacement first, and then controlling the suspension force winding current in the displacement adjustor to achieve accurate control of the radial suspension forces. The *x*-axis and *y*-axis components of the radial suspension forces F_x and F_y in the synchronous rotating *dq*-axis frame can be expressed as

$$\begin{cases} F_x = (K_m + K_l)(i_{s2d}\psi_{1d} + i_{s2q}\psi_{1q}) \\ F_y = (K_m + K_l)(i_{s2q}\psi_{1d} - i_{s2d}\psi_{1q}) \end{cases} \tag{11}$$

where $K_m = \frac{\pi p_1 p_2 L_{m2}}{18\mu_0 l r W_1 W_2}$ and $K_l = \frac{p_1 W_2}{2rW_1}$ are, respectively, the Maxwell forces constant and Lorentz forces constant. ψ_{1d} and ψ_{1q} are, respectively, the *dq*-axis components of air-gap flux linkage of torque windings, i_{s2d} and i_{s2q} are, respectively, the *dq*-axis components of stator current of suspension force windings, L_{m2} is the mutual inductance of suspension force windings, p_2 is the number of pole pairs of suspension force windings, W_1 and W_2 are, respectively, the number of turns of torque windings and suspension force windings, r is the radius of the stator inner surface, l is the length of rotor iron core, and μ_0 is the vacuum permeability.

To achieve steady suspension and operation of the BIM, it is the basic requirement to realize nonlinear decoupling control between electromagnetic torque and radial suspension forces. The vector control is just one of the effective methods. For vector control (in this paper, the vector control refer to the rotor-flux-oriented control if no special statement is given), the rotor flux vector of torque windings is aligned with *d*-axis and setting the rotor flux to be constant equal to the rated flux, which means $\psi_{r1d} = \psi_{r1}$ and $\psi_{r1q} = 0$. Then, the torque winding currents i_{s1d} and i_{s1q}, the slip angular speed ω_s, and the electromagnetic

torque can be expressed as

$$\begin{cases} i_{s1d} = (T_r p_1 + 1)\psi_{r1}/L_{m1} \\ i_{s1q} = T_e L_{r1}/(p_1 L_{m1}\psi_{r1}) \\ \omega_s = \omega_1 - \omega_r = L_{m1} i_{s1q}/(T_{r1}\psi_{r1}) \\ T_e = p_1 L_{m1} i_{s1q}\psi_{r1}/L_{r1}. \end{cases} \tag{12}$$

From (11), it can be seen that the radial suspension forces are related to the air-gap flux of the torque windings; therefore, it can be used to calculate the radial suspension forces only after the air-gap flux is obtained. According to the relationship between air-gap flux and rotor flux, the rotor flux and stator currents of torque windings are utilized to identify the air-gap flux, and the calculating formula can be expressed as follows:

$$\begin{cases} \psi_{1d} = L_{m1}(\psi_{r1d} + L_{r1l} i_{s1d})/L_{r1} \\ \psi_{1q} = L_{m1} L_{r1l} i_{s1q}/L_{r1} \end{cases} \tag{13}$$

where L_{r1l} is the rotor leakage inductance of the torque windings. After the airgap is obtained, the suspension force winding currents can be determined in accordance with (11). By solving (11), we obtain

$$\begin{bmatrix} i_{s2d} \\ i_{s2q} \end{bmatrix} = \frac{1}{M} \begin{bmatrix} \cos\rho & -\sin\rho \\ \sin\rho & \cos\rho \end{bmatrix} \begin{bmatrix} F_x \\ F_y \end{bmatrix} \tag{14}$$

where $M = (K_m + K_l)\sqrt{\psi_{1d}^2 + \psi_{1q}^2}$ and $\rho = \arctan(\psi_{1q}/\psi_{1d})$.

Fig. 5 shows the block diagram of speed-sensorless vector control for the BIM based on ANN inverse speed observer. In the radial position controller, radial positions *x* and *y* are detected by displacement sensors, and then these displacements are compared with the reference values x^* and y^*. The errors are amplified by proportional–integral–derivative controllers to generate the radial suspension force commands F_x^* and F_y^*. In the modulation block described by (14) in Fig. 5, based on radial suspension force commands and sinusoidal and cosinusoidal functions, suspension force winding current commands i_{s2d}^* and i_{s2q}^* are generated so that the actual radial suspension forces follow the radial force suspension commands. These commands i_{s2d}^* and i_{s2q}^* are transformed to instantaneous suspension force winding current commands i_{2A}^*, i_{2B}^*, and i_{2C}^* through the inverse Park transformation and inverse Clark transformation. Then, suspension force winding currents i_{2A}, i_{2B}, and i_{2C} are regulated by a current-regulated pulsewidth modulation (CRPWM)-based inverter using the current commands i_{2A}^*, i_{2B}^*, and i_{2C}^*. Based on the suspension force winding currents, radial suspension force is generated in BIM.

In the motor controller, the rotor speed is observed by the speed observer and the speed error is calculated. The error is amplified in a proportional–integral controller and the electromagnetic torque command T_e^* is generated. By the value absoluting and flux-linkage generator, the rotor speed is transformed to rotor flux-linkage command ψ_{r1}^*. In the modulation block described by (12), the slip angular speed command ω_s^* and torque winding current commands i_{s1d}^* and i_{s1q}^* are generated. These current commands are transformed to instantaneous torque winding current commands i_{1A}^*, i_{1B}^*, and i_{1C}^* through the inverse Park transformation and inverse Clark transformation.

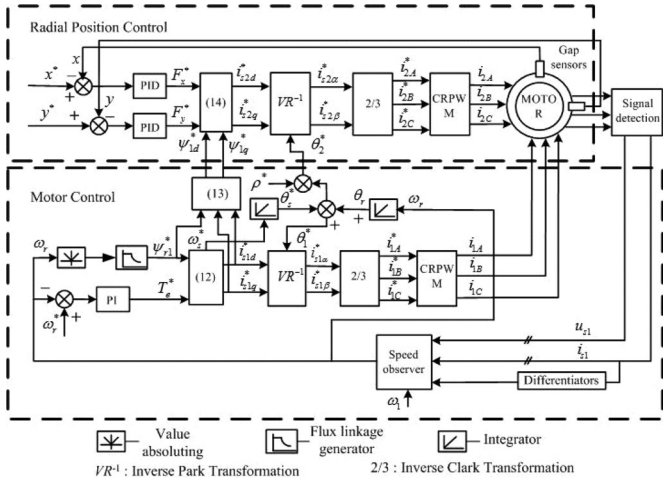

Fig. 5. Block diagram of speed-sensorless vector control for the BIM.

TABLE I
PARAMETERS OF BIM

Parameter	Value	Parameter	Value
L_{s1}	16.778×10^{-2}H	J	0.00769kg·m^2
L_{r1}	16.458×10^{-2}H	p_1	2
L_{m1}	15.856×10^{-2}H	p_2	1
R_{s1}	11.48Ω	m	2.85kg
R_{r1}	11.63Ω		

The rotational angular position θ_r and command θ_s^* are, respectively, integrals of ω_r and ω_s^*. θ_1^* is a sum of θ_s^* and θ_r, and θ_2^* is a sum of θ_1^* and ρ^*. Then, θ_1^* and θ_2^* are used in the inverse Park transformation. Likewise, torque winding currents i_{1A}, i_{1B}, and i_{1C} are regulated by a CRPWM-based inverter using the current commands i_{1A}^*, i_{1B}^*, and i_{1C}^*.

VI. EXPERIMENTS AND ANALYSES

The experimental system consists of a dSPACE DS1104 DSP-based DAC system, a PC, two driving circuit boards with two intelligent power modules, a BIM, an incremental pulse encoder position sensor, and an oscilloscope. The incremental pulse encoder position sensor delivering 2048 pulses per revolution is mounted on the rotor shaft only for comparison of the estimated and real speed of the BIM. The BIM parameters are given in Table I.

Based on the preceding experimental system, we carried out the experiments of speed-sensorless vector control for the BIM system. As is known, it can be used to approximate the nonlinear function $\varphi(\bullet)$ only after the ANN is trained by the training sample. The training data $\{u_{s1d}, u_{s1q}, i_{s1d}, i_{s1q}, \omega_r\}$ were collected under the condition of the BIM vector control, as shown in Fig. 6. With respect to the differentiators appearing in the ANN inversion, it can be realized by using a five-point numerical differential algorithm to guarantee high computing accuracy.

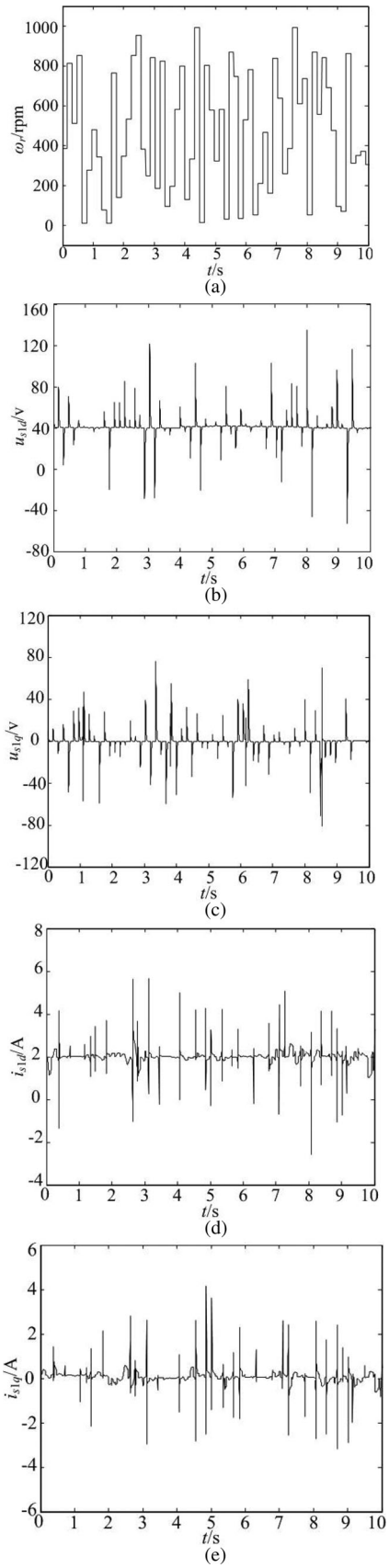

Fig. 6. Collected training data. (a) ω_r. (b) u_{s1d}. (c) u_{s1q}. (d) i_{s1d}. (e) i_{s1q}.

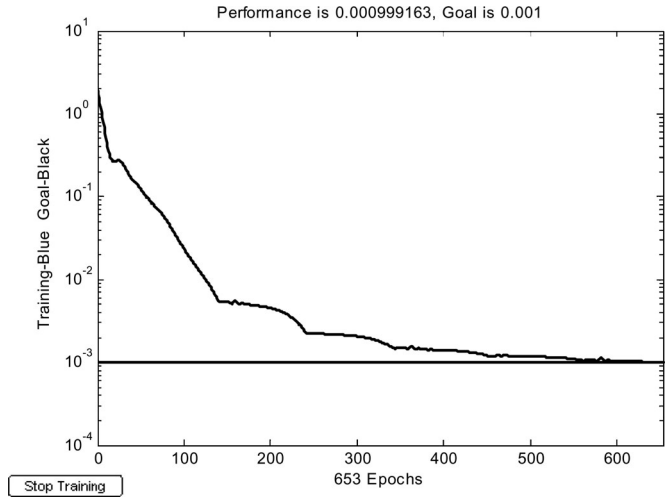

Fig. 7. Training error.

The algorithm's expression can be expressed as

$$\dot{y}_n = \frac{3y_{n-4} - 16y_{n-3} + 36y_{n-2} - 48y_{n-1} + 25y_n}{12\delta}. \quad (15)$$

The basic principle of the five-point numerical differential algorithm is to approach five discrete points with a biquadratic parabola and then calculate its differential. It is more accurate than the conventional two-point numerical algorithm

$$\dot{y}_n = \frac{y_n - y_{n-1}}{\delta}. \quad (16)$$

After the derivatives $\{\dot{i}_{s1d}, \dot{i}_{s1q}\}$ were gained by the five-point numerical differential algorithm, the training sample sets $\{u_{s1d}, u_{s1q}, i_{s1d}, \dot{i}_{s1d}, i_{s1q}, \dot{i}_{s1q}\}$ and $\{\omega_r\}$ were finally obtained. In order to solve the problem of slow convergence, the training data were normalized into $-1 \sim +1$. Based on the training sample set, the weight and threshold of the static ANN can be adjusted using the Levenberg–Marquardt algorithm. After training the static ANN about 653 epochs, the training error was reduced to 9.9916×10^{-4}, and was less than the goal 0.001, which can be seen in Fig. 7.

The trained ANN can then be used to implement the ANN inversion, and accordingly by cascading the original BIM system with the ANN inversion, the desired speed observer can be set up for experiments.

In order to verify the performance of the proposed control algorithm of speed-sensorless vector for the BIM system, several experiment cases were carried out on the various operating conditions. Nonetheless, only the salient results were given notice to in this paper. For comparison, we also gave the corresponding experimental results under the BIM vector control with the incremental pulse encoder position sensor. The experimental results are shown in Figs. 8–11

The results shown in Figs. 8–10 were carried out on the condition of no load. Fig. 8 shows the curves of the estimated speed, actual speed, and the *dq*-axis components of torque winding current in the low-speed operation (50 r/min). From Fig. 8, it can be

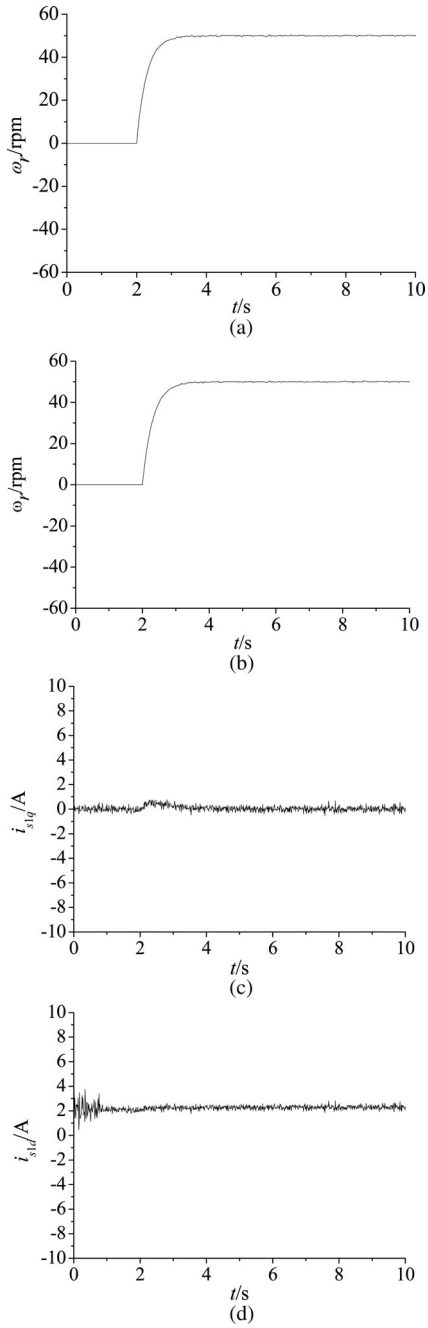

Fig. 8. Experimental results (50 r/min). (a) Estimated speed. (b) Actual speed. (c) $i_{s\,1q}$. (d) $i_{s\,1d}$.

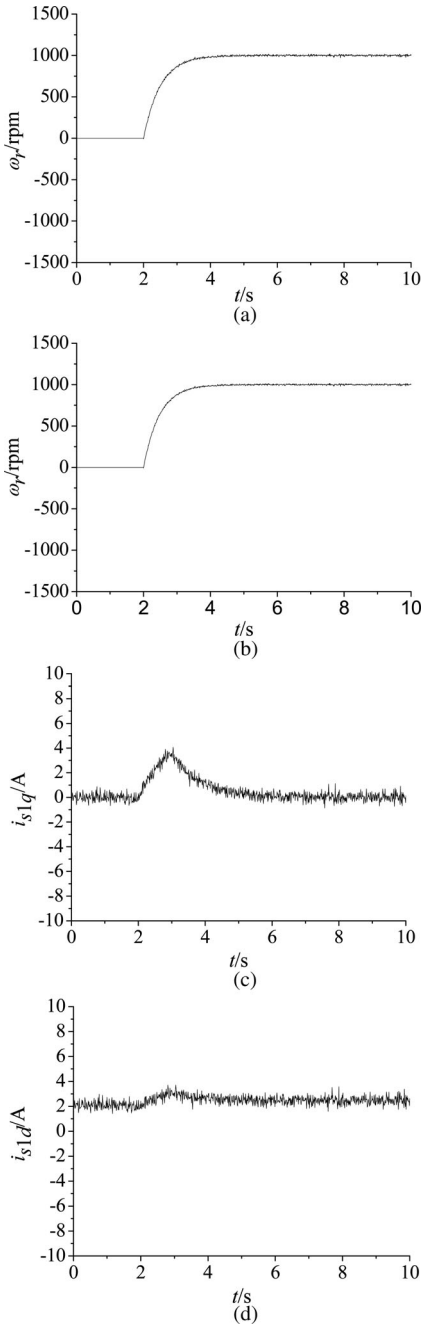

Fig. 9. Experimental results (1000 r/min). (a) Estimated speed. (b) Actual speed. (c) $i_{s\,1q}$. (d) $i_{s\,1d}$.

seen that the BIM system has good speed estimation and high-performance vector control characteristics at low-speed operation by adopting the ANN inverse speed observer. Fig. 9 shows the curves of the estimated speed, actual speed, and currents at 1000 r/min reference speed. As in the low-speed region, the BIM system also show high performance at the speed of 1000 r/min. Fig. 10 shows the results of variable-speed control performance from 600 to -600 r/min reference speed. From Fig. 10, we can see that good static and dynamic performance of the variable-speed control can be obtained. In Figs. 8–10, it is seen that the q-axis component of torque winding current $i_{s\,1q}$ is almost zero when the system is at steady operating state because there is no load. In order to further study the control performance, we apply the load to the BIM system at 300 r/min speed, and the results are shown in Fig. 11. From Fig. 11, it can be seen that the estimated speed is also in accordance with the actual one exactly with load. The comparison between the estimated speed and actual one is shown in Table II. From the comparative results, we can see that the BIM system has good control performance from low speed to the speed range of 1000 r/min by using the proposed speed-sensorless control algorithm.

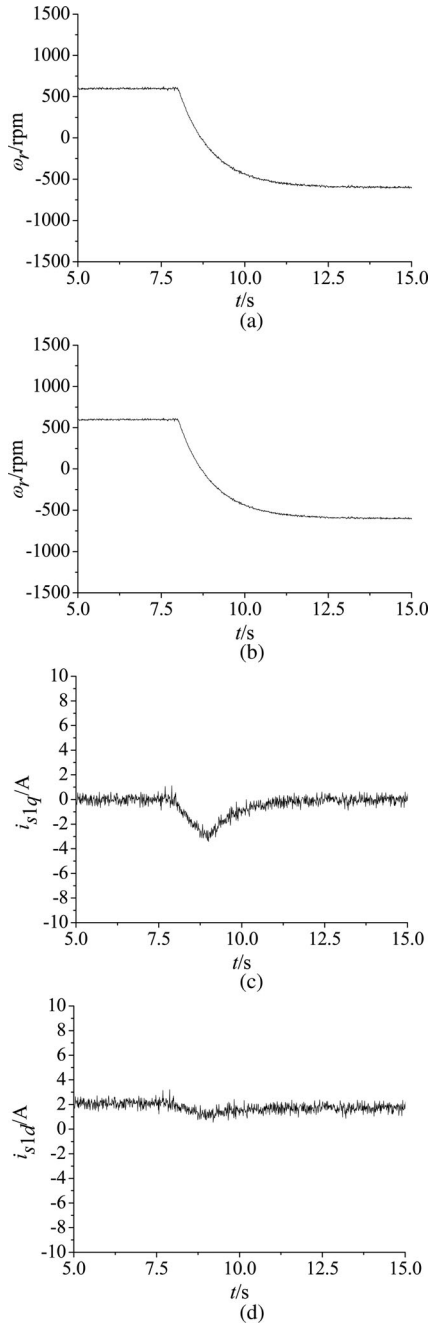

Fig. 10. Experimental results (−600–600 r/min). (a) Estimated speed. (b) Actual speed. (c) $i_{s\,1q}$. (d) $i_{s\,1d}$.

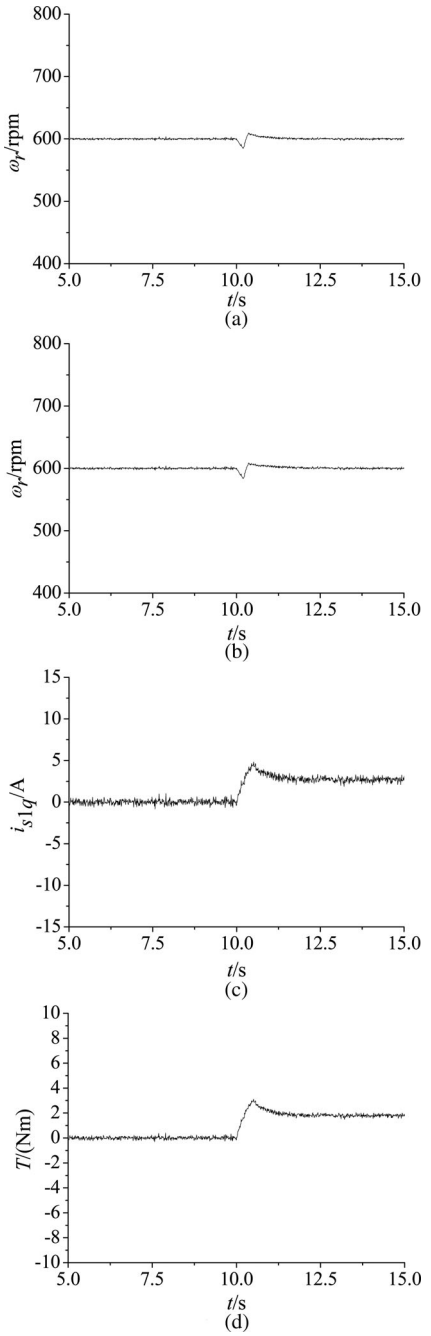

Fig. 11. Experimental results (600 r/min with load). (a) Estimated speed. (b) Actual speed. (c) $i_{s\,1q}$. (d) T.

TABLE II
COMPARISON BETWEEN THE ESTIMATED SPEED AND THE ACTUAL ONE

Reference speed (rpm)	Measured speed (rpm)	Actual speed (rpm)
5	5.03	5.04
50	99.07	100.06
600	597.88	601.32
1000	995.42	1000.86

VII. CONCLUSION

In this paper, a novel speed-sensorless vector control of a BIM drive with the ANN inverse speed observer has been developed and described, and the drive system has also been implemented by using a dSPACE DS1104 DSP-based DAC system. Experimental results have shown that the proposed algorithm is able to estimate the speed exactly for a wide speed range. Particularly, good robust and speed estimation performances have been obtained at load variation or variable-speed operation. Meanwhile, all experimental results have confirmed good dynamic

performance and stability of the BIM drive system, and shown the validity and feasibility of the proposed speed-sensorless vector control algorithm. Moreover, the ANN inverse speed observer realized in software will not increase total system cost, which makes the drive system suitable to be used in practical engineering.

REFERENCES

[1] T. Reichert, T. Nussbaumer, and J. W. Kolar, "Bearingless 300-W PMSM for bioreactor mixing," *IEEE Trans. Ind. Electron.*, vol. 59, no. 3, pp. 1376–1388, Mar. 2012.

[2] H. Grabner, W. Amrhein, S. Silber, and W. Gruber, "Nonlinear feedback control of a bearingless brushless DC motor," *IEEE/ASME Trans. Mechatronics*, vol. 15, no. 1, pp. 40–47, Feb. 2010.

[3] A. Chiba and J. A. Santisteban, "A PWM harmonics elimination method in simultaneous estimation of magnetic field and displacements in bearingless induction motors," *IEEE Trans. Ind. Appl.*, vol. 48, no. 1, pp. 124–131, Jan./Feb. 2012.

[4] Z. Qi, P. C. Liang, M. Y. Ting, K. F. Rang, and F. Z. Hua, "Piezoelectric rotary motor based on active bulk torsional element with grooved helical electrodes," *IEEE/ASME Trans. Mechatronics*, vol. 17, no. 2, pp. 260–268, Apr. 2012.

[5] M. S. Huang, Y. L. Hsu, and R. F. Fung, "Minimum-energy point-to-point trajectory planning for a motor-toggle servomechanism," *IEEE/ASME Trans. Mechatronics*, vol. 17, no. 2, pp. 337–344, Apr. 2012.

[6] Y. M. Choi and D. G. Gweon, "A high-precision dual-servo stage using Halbach linear active magnetic bearings," *IEEE/ASME Trans. Mechatronics.*, vol. 16, no. 5, pp. 925–931, Oct. 2011.

[7] T. Schuhmann, W. Hofmann, and R. Werner, "Improving operational performance of active magnetic bearings using Kalman filter and state feedback control," *IEEE Trans. Ind. Electron.*, vol. 59, no. 2, pp. 821–829, Feb. 2012.

[8] I. U. R. Usman, M. Paone, K. Smeds, and X. D. Lu, "Radially biased axial magnetic bearings/motors for precision rotary-axial spindles," *IEEE/ASME Trans. Mechatronics*, vol. 16, no. 3, pp. 411–420, Jun. 2011.

[9] G.-J. Yan, L.-Y. Hsu, J.-H. Wang, M.-C. Tsai, and X.-Y. Wu, "Axial-flux permanent magnet brushless motor for slim vortex pumps," *IEEE Trans Magn*, vol. 45, no. 10, pp. 4732–4735, Oct. 2010.

[10] T. Nussbaumer, P. Karutz, F. Zurcher, and J. W. Kolar, "Magnetically levitated slice motors—an overview," *IEEE Trans. Ind. Appl.*, vol. 47, no. 2, pp. 754–766, Mar./Apr. 2011.

[11] A. Chiba, T. Fukao, O. Ichikawa, M. Oshima, M. Takemoto, and D. G. Dorrell, *Magnetic Bearings and Bearingless Drives*. Oxford, U.K.: Elsevier, 2005.

[12] A. Chiba, T. Fukao, and M. A. Rahman, "Vibration suppression of a flexible shaft with a simplified bearingless induction motor drive," *IEEE Trans. Ind. Appl.*, vol. 44, no. 3, pp. 745–752, May/Jun. 2008.

[13] S. Zhang and F. Luo, "Direct control of radial displacement for bearingless permanent-magnet-type synchronous motors," *IEEE Trans. Ind. Electron.*, vol. 56, no. 2, pp. 542–552, Feb. 2009.

[14] T. Schneeberger, T. Nussbaumer, and J. W. Kolar, "Magnetically levitated homopolar hollow-shaft motor," *IEEE/ASME Trans. Mechatronics*, vol. 15, no. 1, pp. 97–107, Feb. 2010.

[15] D. N. Quang and U. Satoshi, "Modeling and control of salient-pole permanent magnet axial-gap self-bearing motor," *IEEE/ASME Trans. Mechatronics*, vol. 16, no. 3, pp. 518–526, Jun. 2011.

[16] G. Yang, Z. Deng, X. Cao, and X. Wang, "Optimal winding arrangements of a bearingless switched reluctance motor," *IEEE Trans. Power Electron.*, vol. 23, no. 6, pp. 3056–3066, Nov. 2008.

[17] B. Akin, U. Orguner, A. Ersak, and M. Ehsani, "Simple derivative-free nonlinear state observer for sensorless ac drives," *IEEE/ASME Trans. Mechatronics*, vol. 11, no. 5, pp. 634–643, Oct. 2006.

[18] S. B. Ozturk and H. A. Toliyat, "Direct torque and indirect flux control of brushless dc motor," *IEEE/ASME Trans. Mechatronics*, vol. 16, no. 2, pp. 351–360, Apr. 2011.

[19] R. M. Bharadwaj and A. G. Parlos, "Neural speed filtering for induction motors with anomalies and incipient faults," *IEEE/ASME Trans. Mechatronics*, vol. 9, no. 4, pp. 679–688, Aug. 2004.

[20] P. Krishnamurthy and F. Khorrami, "Robust adaptive control of sawyer motors without current measurements," *IEEE/ASME Trans. Mechatronics*, vol. 9, no. 4, pp. 689–696, Aug. 2004.

[21] P. Vas, *Sensorless Vector and Direct Torque Control*. New York: Oxford Univ. Press, 1998.

[22] S. Hasan and I. Husain, "A Luenberger-sliding mode observer for online parameter estimation and adaptation in high-performance induction motor drives," *IEEE Trans. Ind. Appl.*, vol. 45, no. 2, pp. 772–781, Mar./Apr. 2009.

[23] T. S. Kwon, M. H. Shin, and D. S. Hyun, "Speed sensorless stator flux-oriented control of induction motor in the field weakening region using Luenberger observer," *IEEE Trans. Power Electron.*, vol. 20, no. 4, pp. 864–869, Jul. 2005.

[24] M. Barut, S. Bogosyan, and M. Gokasan, "Speed-sensorless estimation for induction motors using extended Kalman filters," *IEEE Trans. Ind. Electron.*, vol. 54, no. 1, pp. 272–280, Feb. 2007.

[25] M. Barut, S. Bogosyan, and M. Gokasan, "Experimental evaluation of braided EKF for sensorless control of induction motors," *IEEE Trans. Ind. Electron.*, vol. 55, no. 2, pp. 620–632, Feb. 2008.

[26] T. Orlowska-Kowalska and M. Dybkowski, "Stator-current-based MRAS estimator for a wide range speed-sensorless induction-motor drive," *IEEE Trans. Ind. Electron.*, vol. 57, no. 4, pp. 1296–1308, Apr. 2010.

[27] S. M. Gadoue, D. Giaouris, and J. W. Finch, "MRAS sensorless vector control of an induction motor using new sliding-mode and fuzzy-logic adaptation mechanisms," *IEEE Trans. Energy Convers.*, vol. 25, no. 2, pp. 384–402, Jun. 2010.

[28] X. Dai, D. He, and X. Zhang, "MIMO system invertibility and decoupling control strategies based on ANN αth-order inversion," *Proc. Inst. Elect. Eng.—Control Theory Appl.*, vol. 148, no. 2, pp. 125–136, Mar. 2001.

[29] X. Dai, M. Yin, Q. Wang, and W. Wang, "Artificial neural networks inversion based dynamic compensator of sensors," in *Proc. Int. Conf. Inf. Acquisition*, 2004, pp. 258–261.

[30] C. M. Kwan and F. L. Lewis, "Robust backstepping control of induction motors using neural networks," *IEEE Trans. Neural Netw.*, vol. 11, no. 5, pp. 1178–118, Sep. 2000.

[31] R. Walter, *Principles of Mathematical Analysis*. New York: McGraw-Hill, 1976.

[32] V. Kùrková, "Kolmogorov's theorem and multilayer neural networks," *Neural Netw.* vol. 5, no. 3, pp. 501–506, 1992.

[33] M. Hagan, H. Demuth, and M. Beale, *Neural Network Design*. Boston, MA: PWS-Kent, 1996.

[34] X. Sun, H. Zhu, and W. Pan, "Decoupling control of bearingless permanent magnet-type synchronous motor using artificial neural networks-based inverse system method," *Int. J. Model. Ident. Control*, vol. 8, no. 2, pp. 114–121, Sep. 2009.

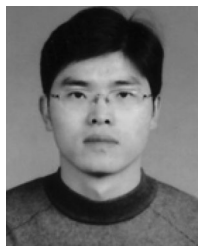

Xiaodong Sun was born in Jiangsu, China, in 1981. He received the B.Sc. degree in electrical engineering and the M.Sc. and Ph.D. degrees in control engineering from Jiangsu University, Zhenjiang, China, in 2004, 2008, and 2011, respectively.

Since 2004, he has been with Jiangsu University, where he is currently a Lecturer with the Automotive Engineering Research Institute. His research interests include bearingless motors, motor drives and control, drives for electric vehicles, and intelligent control.

Long Chen was born in Jiangsu, China, in 1958. He received the B.Sc. and Ph.D. degrees in mechanical engineering from Jiangsu University, Zhenjiang, China, in 1982 and 2006, respectively.

He is currently a Professor in the Automotive Engineering Research Institute, Jiangsu University. His research interests include electric vehicles, electric drives, simulation and control of vehicle dynamic performance, vehicle operation, and transport planning.

Zebin Yang was born in Hubei, China, in 1976. He received the B.Sc. and M.Sc. degrees in electrical engineering from Jiangsu University, Zhenjiang, China, in 1999 and 2004, respectively, where he is currently working toward the Ph.D. degree.

He is currently an Associate Professor in the School of Electrical and Information Engineering, Jiangsu University. His research interests include control engineering and filtering, singular linear systems, and intelligent control of special motors.

Huangqiu Zhu was born in Jiangsu, China, in 1964. He received the Ph.D. degree in mechanical engineering from Nanjing University of Aeronautics and Astronautics, Nanjing, China, in 2000.

He is currently a Professor in the School of Electrical and Information Engineering, Jiangsu University, Zhenjiang, China. His research interests include magnetic bearings, magnetic suspension (bearingless) motors, motor's movement control, etc.